Interchangeable use of GNSS and seismic data for rapid earthquake characterization: 2021 Chignik earthquake, Alaska

Revathy M. Parameswaran[1]*, Ronni Grapenthin[1], Michael West[1], Alex Fozkos[1]

[1]Geophysical Institute, University of Alaska Fairbanks, Fairbanks, AK, 99775

*Corresponding author: rmparameswaran@alaska.edu

Declaration of Competing Interests

The authors acknowledge there are no conflicts of interest recorded.

Abstract: (300 words)

Earthquake magnitude estimation using peak ground velocities (PGV) derived from Global Navigation Satellite Systems (GNSS) data has shown promise for rapid characterization of damaging earthquakes. Here we examine the feasibility of using GNSS-derived velocity waveforms as interchangeable data for ground motion estimation and other products that typically rely on strong-motion seismic records. Our study compares PGVs derived from high-rate GNSS to those computed from high-rate seismic records (strong-motion and velocity), at co- and closely-located stations. The recent 2021

Mw 8.2 Chignik earthquake in Alaska that was recorded on co-located GNSS and strong-motion sensors provides the perfect opportunity to compare the two data streams and their application in rapid response. The Chignik velocity records appear almost identical at co-located GNSS and strong-motion stations when observed at frequencies < 0.25 Hz. GNSS and strong-motion derived velocity data are further employed to generate rapid estimates of PGV-derived moment magnitudes for the earthquake. The moment magnitude estimates from GNSS and joint GNSS/seismic data are within ~ ±0.4 magnitude units (Fang et al., 2020) of the final magnitude (Mw 8.2). ShakeMaps generated for the 2021 Chignik earthquake using GNSS and seismic PGVs show notable agreement between them, and show negligible shifts in PGV contours when co-/closely located GNSS and seismic stations are substituted for one another. Therefore, we posit that GNSS is a powerful alternative or addition to seismic data and vice versa.

Keywords:

Earthquake rapid response, GNSS, strong-motion, Chignik earthquake, ShakeMaps

Key Points:

- GNSS and seismic ground velocities for the 2021 Chignik earthquake are the same within ~0.25 Hz in co-located GNSS and seismic stations.

- PGV-magnitudes using GNSS and joint GNSS/seismic data, within GNSS frequency bands, are within ~±0.4 magnitude units of uncertainty (Fang et al. (2020).

- Ground motion estimates using GNSS and seismic data are comparable; even when co-located stations are interchanged.

Introduction

Joint approach to earthquake rapid response

Along most subduction zones, seismic risk and damage estimation associated with large earthquakes depend on rapid, accurate evaluation of earthquake magnitude and associated ground shaking. Regions prone to high seismic risk could benefit from simultaneous (to increase accuracy) or interchangeable (in the event that either type of data is unavailable or inoperative) use of seismic and geodetic data for rapid earthquake detection and characterization. From an operational perspective for earthquake early warning (EEW), early detection using P-wave arrivals in the immediate vicinity of an earthquake is a widely used method (e.g., Kuyuk et al., 2014; Given et al., 2014; Rinehart et al., 2016). Meanwhile, rapid earthquake characterization relies on incoming S-waves, where the focus is also on estimating the magnitude, depth, and the area of impact, accommodating for the full rupture, besides event detection (e.g., Grapenthin et al., 2014a,b; 2017; Crowell et al., 2016). Over the last two decades, high-rate GNSS (>=1 Hz) have become mature enough to detect and characterize earthquakes in real time. These high-rate GNSS position data can be used in conjunction with positions estimated by double-integrating accelerations from co-located high-rate strong-motion instruments through a Kalman filter to create displacement data-streams of millimeter-scale precision (Bock et al., 2011). Peak ground displacements (PGDs) derived from high-rate GNSS time series have been effectively used in rapid magnitude estimation for large earthquakes using PGD-magnitude scaling relationships (e.g., Crowell et al., 2013, Grapenthin et al., 2014b; Melgar et al., 2016; Grapenthin et al., 2017). A different approach would be to characterize earthquakes using coseismic ground velocities. This was successfully illustrated by computing instantaneous receiver velocities (or '*instavels*') for large earthquakes from high-rate GNSS data (Colosimo et al., 2011; Grapenthin et al., 2018). The advantages of using instavels are that they can be rapidly computed using single frequency GNSS data, ultra-rapid orbits, and no atmospheric/ionospheric models (Colosimo et al., 2011; Grapenthin et al., 2018). Akin to PGDs, peak ground velocities (PGVs) derived from instavels can also be scaled to magnitude and hypocentral distances by constraining attenuation relationships, and can be used for rapid earthquake characterization (Fang et al., 2020). Grapenthin et al. (2018) illustrate that PGVs derived from instavels when subjected to PGV-magnitude scaling relationships can be incorporated into ground motion products such as ShakeMaps. However, it is important to evaluate how instavels compare to strong-motion/seismic velocity observations to establish coherence between the two data types. Our hope is to provide a quantitative foundation describing the applications for which GNSS and strong-motion seismic data can be used interchangeably or in combination, and what the caveats are (e.g., PGV-derived magnitude estimates, ground motion intensity maps, etc.). The 2021 Mw 8.2

Chignik earthquake provided an ideal test case to examine the interchangeability of GNSS and seismic data in rapid earthquake characterization.

The size and location of the July 29, 2021, Mw 8.2 Chignik earthquake in Alaska provided a rare opportunity to reconcile GNSS observations with their seismic counterparts. The earthquake was the largest event in more than 50 years along the Aleutian megathrust, and the earthquake epicenter was in the vicinity of co- or closely-located GNSS and seismic stations, inducing signals well above the noise floor of the observing instrumentation. In this paper, we examine geodetic and seismic velocity records of the earthquake and how they compare. Furthermore, we assess the relationship between hypocentral distance and PGVs with the rapid magnitude estimates derived from both GNSS and seismic velocities. Lastly, we explore the effectiveness of GNSS observations as an alternate and complementary dataset that can be incorporated into ground motion estimation products. The ground motion models can be generic or region specific; an example of the latter would be those used in Japan, for instance (e.g., Koketsu et al., 2008; Morikawa and Fujiwara, 2013). In this study we model ground motion using the ShakeMap program (Worden et al., 2012).

The 2021 Mw 8.2 Chignik earthquake

The 2021 Mw 8.2 Chignik earthquake in Alaska was the largest earthquake in the United States since the 1965 M8.7 Rat Island event (Stauder, 1968; Wu and Kanamori, 1973; Elliott et al., 2022). The earthquake occurred along the Alaska-Aleutian subduction zone, where the Pacific plate underthrusts the North American plate. The subduction zone is noted for its high seismic productivity and variable coupling (e.g., Sykes et al. 1981;

Drooff & Freymueller, 2021) (Figure 1). Segments of the subduction arc close to the Alaskan Peninsula and the eastern Aleutian Islands have witnessed several large earthquakes in recorded history. The 1964 M9.2 Prince William Sound earthquake (e.g., Ichinose et al., 2007; Benz et al., 2011), the 1938 M8.3 Alaska Peninsula earthquake (e.g., Johnson and Satake, 1994), and the 1946 M7.4 Sanak earthquake (M8.6 based on the magnitude of the ensuing tsunami) (e.g., López and Okal, 2006) are a few of the larger events to strike this subduction zone. However, the area stretching across the Shumagin Islands, sandwiched between the 1938 and 1946 events, does not have a clear history of great earthquakes, and has been known as the 'Shumagin seismic gap' (Davies et al., 1981; Witter et al., 2014). This is no longer the case since the July 22, 2020 Mw 7.8 Simeonof earthquake ruptured deeper portions of the megathrust below the continental shelf (Crowell & Melgar, 2020; Liu et al., 2020; Xiao et al., 2021; Ye et al., 2021). To its east-northeast, the Simeonof event was followed by the 2021 Mw 8.2 Chignik earthquake, which seems to have ruptured the western two-thirds of the 1938 Alaska Peninsula earthquake aftershock zone, with little evidence of it being a repeat of the 1938 event (Elliott et al., 2022; Liu et al., 2022; Ye et al., 2022). Together with the 2020 Simeonof earthquake, the Chignik event seems to have closed the deeper parts of the Shumagin gap (Elliott et al., 2022). We choose the 2021 Chignik earthquake in this study because of: (1) the size of the earthquake and associated ground motions; (2) the proximity to functional and well-maintained seismic and geodetic networks; and (3) most importantly, the existence of co-located seismic and geodetic stations.

Methodology and Results

We start by identifying GNSS stations that continuously recorded high-rate data during the Chignik earthquake and are located within 600 km from the epicenter. The GNSS instrumentation comprises stations that operate at 1Hz and/or 5Hz sampling rate, of which we use the 1 Hz data for consistency in analysis. We then proceed to select seismic stations that are co-/closely located to the GNSS stations identified here. The seismic instrumentation comprises two types - broadband and strong-motion. The broadband sensors are weak-motion instruments designed to record small ground motions with high signal-to-noise and high fidelity across a wide range of frequencies. Broadband data are natively recorded in velocity. However, the strong ground motions near large earthquakes exceed the dynamic range and amplitude limits of most broadband sensors. To help account for this, strong-motion accelerometers are deployed to complement broadbands. Most strong-motion sensors record natively in acceleration. Within the defined bounds, 3 strong-motion stations (AK.S15K, AK.CHN, AK.S19K) are co-/closely-located to 3 of the selected GNSS receivers (AB13, AC12, AC34). Of the operational GNSS and strong-motion stations, two pairs are co-located, while another is closely located (<2 km). There are several broadband stations (for e.g., AV.DOL, AK.P16K, AV.PS1A, AV.PS4A, AV.SSLN, AV.WESE etc) that are at comparable hypocentral distances as the GNSS stations. However, we primarily focus on the strong-motion records to avoid data saturation in broadband velocity data (Figure S1 in the electronic supplement).

Traditionally, GNSS data is considered in displacement space while strong-motion sensors natively record in acceleration. We choose to compare the datasets in velocity space for a number of reasons. Unlike position data, GNSS receiver velocities or instavels can be estimated directly from GNSS satellite phase and range observations. This reduces the complexity arising from multiple time derivatives and externally obtained corrections (Misra and Enge, 2011), resulting in records without amplitude saturation (unlike seismic velocity records) from these non-inertial sensors. Double integrating strong-motion acceleration records to produce displacement is problematic since the static integration term (arguably the core strength of GNSS) is lost. Lastly, the comparatively low, currently prevalent sample rate of GNSS (1 Hz) means that frequencies above 0.5 Hz are not recorded. This impact would be exacerbated by differentiating the GNSS to acceleration. For these reasons, velocity provides a middle ground for comparing these data that minimizes the caveats on both data types.

Instantaneous GNSS velocities: Instavels

Instantaneous GNSS receiver velocities or instavels are derived from the Doppler shift observed in the carrier phase change that results from both satellite and receiver motion. When the satellite trajectory is smooth or well known (e.g., Benedetti et al., 2014; Grapenthin et al., 2018) the change in the observed frequency of the satellite signal primarily represents the receiver velocity (Misra and Enge, 2011). Phase-velocity (Doppler shift) observations for a GNSS receiver are computed assuming that ionosphere and troposphere are static over short time periods (≤ 1s) and no cycle slips occur (Misra and Enge, 2011; Gaglione, 2015). We can infer this from differenced subsequent carrier phase observations, $\Delta\phi^s$:

$$\Delta\phi^s = (v^s - v_r) \times 1^s + \hat{b} + \delta\epsilon_\phi \quad (1)$$

where $(v^s - v_r) \times 1^s$ is the range difference between the velocity v^s of satellite *s*, which is known and can thus be removed, and velocity v_r of receiver *r,* projected onto the receiver-to-satellite line of sight with the respective unit vector 1^s. The terms $\hat{b}$ and $\delta\epsilon_\phi$ are the shifts in satellite/receiver clock biases and error terms, respectively. The Doppler shifts observed from at least four satellites due to the receiver moving at velocity v_r, is given by:

$$\mathbf{D} = \mathbf{G}\ [\mathbf{v_r}\ \hat{b}_r]^T + \delta\epsilon_\phi \quad (2)$$

where **D** is a vector of Doppler shift observations and **G** is the system matrix that contains unit vectors to project the receiver velocities $\mathbf{v_r} = [v_x\ v_y\ v_z]^T$ onto the line of sight to the satellite. The instavels are calculated in an Earth-centered, Earth-fixed Cartesian coordinate system and then rotated into a local east–north–up reference frame. Equation (2) is solved for $\mathbf{v_r}$ and $\hat{b}_r$ (receiver clock bias) using standard least-squares techniques (e.g., Aster et al., 2018), and observation weights are removed based on satellite elevation angles in the inversion. We consider and compare observations from a combination of L1 (1575.42 MHz) and L2 (1227.6 MHz) transmission frequencies, and using L2 alone.

Seismic vs instavel comparison for co-located stations

The GNSS data used in the study are limited to 1Hz sampling rates, while seismic data are sampled at 50-100 Hz. To facilitate direct comparison, we resample the seismic data to a common sampling rate (1Hz). We achieve this by correcting for instrument response in the seismic data followed by resampling it to the 1Hz GNSS timestamps using the ObsPy framework (Beyreuther et al., 2010; Megies et al., 2011; Krischer et al., 2015).

We use Coordinated Universal Time (UTC) timestamps for the seismic data. The UTC is defined based on atomic clocks, and the corrections associated with Earth's rotation are incorporated into them. Meanwhile, the clocks on Global Positioning System (GPS) satellites, which we use to procure GNSS data for this study, were calibrated to UTC in 1980, but don't account for corrections from that point onwards. Therefore, integer corrections called 'leap seconds' are introduced at appropriate times to account for variations from UTC (e.g., Lewandowski and Arias, 2011). Here, the GNSS data are timeshifted by +18 seconds for the year 2021. At the 'seconds' mark, the raw GNSS and seismic timestamps deviate from one another by an order of 10E-3 seconds. This deviation is considerably lower than the individual sampling rates. Therefore, we neglect this difference instead of accounting for the deviation through interpolation approaches. The strong-motion data is subsequently subjected to trapezoidal first-order integration using ObsPy to obtain corresponding velocities.

The re-sampled seismic velocity traces are then compared to their GNSS instavel counterparts with the objective of identifying (a) commonalities that represent the Chignik earthquake and (b) the frequencies at which the GNSS produce faithful ground motion records for this event. We start by subtracting the seismic time series from the GNSS instavels (Figure 2a bottom). Subsequently, we generate spectrograms for each of the time series - seismic, instavel, and differenced records - as illustrated in Figure 2b. The spectrograms allow us to identify frequency bands with common energy distributions. For the station pair AC34 (GNSS) and AK.S19K (strong-motion) (henceforth identified as station pair AC34:S19K - GNSS:strong-motion), we observe highly similar signals within the frequency range 0.001-0.25Hz. However, at frequencies above ~0.25Hz we observe energy in the instavels that does not appear in the strong-motion record. We attribute this to spurious noise in the GNSS data. The spectrogram of the signal difference (Figure 2b, bottom) further confirms that the two signals are most similar below 0.25 Hz. To examine the coherence of the signal that is common to both records, we bandpass filter the data at 0.001-0.25Hz (Figure 3, top, middle), and then cross-correlate the filtered time series (Figure 3, bottom). The peak of the cross-correlation function provides an objective measure of similarity. The lag time associated with the cross-correlation peak reveals whether or not the processing introduces meaningful time shifts (Figures 3a,b,c).

We apply this method to the two other co-located GNSS-seismic station pairs - AC34:S19K (Figures 2 and 3) and AC12:CHN (Figure S2 in the electronic supplement), and closely located stations AB13:S15K that are separated by ~2 km (Figure S3 in the electronic supplement). These three comparisons suggest that a large portion of the Chignik earthquake signal is captured in the GNSS records in the 0.001 to 0.25 Hz frequency band (Figures 2 and 3; Figures S2 and S3). Co-located stations AC34:S19K show a high correlation of 0.9 and a lag of -1s (E-component) (Figure 3a). The second pair of co-located stations AC12:CHN show a correlation of 0.77 and a lag of -1s (Figure S2 in the electronic supplement). Closely-located stations AB13:S15K show a wider range of frequency content in their spectrogram and show lower correlation (cross-correlation = 0.6; lag = 0s) compared to the co-located stations (Figure S3 in the electronic supplement).

PGV-derived magnitude: GNSS, Seismic, Joint

Fang et al. (2020) proposed a method to estimate earthquake magnitudes using PGVs derived from instavels. They developed attenuation relationships for PGVs with respect to hypocentral distances using over 1434 records from 22 earthquakes worldwide. They used these attenuation relationships to constrain an empirical PGV-magnitude scaling law. The 3D or 2D (horizontal-only) PGV from a three-component instavel waveform is given by:

$$PGV_{total} = \max\,(v_n^2 + v_e^2 + v_u^2)^{1/2} \quad (3)$$

$$PGV_{horizontal} = \max\,(v_n^2 + v_e^2)^{½} \quad (4)$$

where v_n, v_e, and v_u are the north, east, and up velocity waveforms, respectively.

Fang et al. (2020) formulated the moment magnitude (M_w) calculation based on the following scaling law between PGVs and hypocentral distances (R)

$$\log(PGV) = A + B \times M_w + C \times M_w \times \log(R) \quad (5)$$

where A = −5.025 ± 0:084, B = 0.741 ± 0.017, C = −0.111 ± 0.003 are the regression coefficients, and the standard deviation of the magnitude residual (predicted minus actual magnitudes) is ± 0.389 (~±0.4) magnitude units.

We produce PGVs from the unfiltered (up to 0.5 Hz; Nyquist frequency for 1Hz sampling) seismic and GNSS velocity time series (Table 1) and implement the Fang et al. (2020) PGV scaling relationships for magnitude estimation for the 2021 Chignik earthquake. To simulate a real-time environment, we recalculate PGV at each timestep, effectively creating PGV time series that monotonically increases toward the global PGV for each station (listed in Table 1) and remains constant after that. Using these PGV time series, we determine the moment magnitude evolution from instavels and seismic PGVs individually, and as a combined dataset (GNSS+seismic). For an effective comparison, we first compute rapid estimates of magnitude using all 22 GNSS stations, followed by magnitude estimates using the strong-motion stations alone, and then using both GNSS (22) and strong-motion (3) stations. The instavels are computed using L2 and L1+L2 frequency bands, of which we prefer to use the results obtained using the L2 frequencies (Figure 4) due to the larger noise levels in L1 frequencies, although the final magnitude estimates are comparable. Figure 4a shows the evolution of moment magnitude from instavels (22 stations; L2 and L1+L2), strong-motion (3 stations), and combined data (22 instavels and 3 strong-motion records), with moment release over time. Figure 4b represents the scaling relation between the hypocentral distances and the GNSS and strong-motion PGVs (Table 1) for the estimated moment magnitude. PGVs obtained from all 22 GNSS stations result in a final moment magnitude of Mw 8.06 (using L2; Mw 7.97 using L1+L2), within uncertainty bounds of ~±0.4 magnitude units from the final magnitude (Mw 8.2), as prescribed by the scaling relationships. The PGVs from strong-motion records result in a final value of Mw 7.78, while the joint GNSS (22 stations) and strong-motion (3 stations) moment magnitude arrives at Mw 7.9. Based on results from GNSS and strong-motion stations, the PGV-derived moment magnitudes are within the predicted standard deviations (~±0.4) of magnitude units (Fang et al., 2020).

GNSS and seismic ShakeMaps

We use the operational ShakeMap configuration (Worden et al., 2012) at the Alaska Earthquake Center to assess the possibility of using instavels as an alternative or in addition to seismic input for ShakeMaps. The ShakeMap methodology uses location-specific ground motion models to forward model estimated shaking. Instrumental records are then used to adjust and correct these estimates. The more instrumental observations that are incorporated into ground motion products, the more accurate and precise the output is. These instrumental records may comprise peak ground accelerations (PGA) and/or peak ground velocities (PGV). We compare ShakeMaps generated using instavel PGVs to those obtained from the filtered seismic velocities. ShakeMaps, as produced at the Alaska Earthquake Center are based on 0.1Hz highpass filtered seismic records to compute the shaking intensity and PGV contours. We further use ShakeMap to derive PGV contours using PGVs (Table 1) from identically sampled GNSS and seismic records.

Figure 5 presents PGV contours generated from - (a) 1 Hz co-/closely-located GNSS instavels (3 records), (b) downsampled 1 Hz co-/closely-located strong-motion data (3 stations), (c) 1 Hz GNSS instavels (22 records), (d) 1 Hz GNSS instavels replaced with co-/closely-located downsampled strong-motion data. The corresponding ShakeMaps (with color gradients instead of the PGV contours in Figure 5) and the official ShakeMap released by USGS can be found in Figure S4 of the electronic supplement. We observe that the PGV contours derived from the co-/closely-located GNSS and strong-motion stations are more-or-less identical (Figure 5a,b). Meanwhile, the 20 cm/s PGV contour synthesized using all 22 instavels (Figure 5c) shrinks by ~50 km from those generated using the 3 strong-motion stations (Figure 5a). The 10 cm/s contour also shows some shrinkage, albeit lesser, in the instavel PGVs compared to their seismic counterparts. Meanwhile, PGVs contours <10 cm/s (>200 km from the epicenter) for both cases mimic one another remarkably. The test cases illustrated in Figures 5d show that substituting GNSS stations with co-/closely-located strong-motion stations, and potentially vice versa, result in negligible changes in the extents of the PGV contours compared to the original, unsubstituted sets (Figures 5c).

Discussion

One of the key observations from this study is that the seismic and GNSS PGVs closely correlate at GNSS frequencies (the frequency band at which the GNSS time series effectively records ground motion with fidelity; in this case, 1Hz data) at co-located stations for the 2021 Mw 8.2 Chignik earthquake. This is evident from Figures 2 and 3 that compare the AC34 instavel to the seismic trace from AK.S19K. The spectrograms of the unfiltered 1Hz velocity time series show comparable energy distribution <0.25 Hz. A similar energy concentration was found in the case of the second co-located station-pair, AC12:CHN, and the resultant correlation between the filtered data is also high (Figure S2 in the electronic supplement). Meanwhile, closely-located station pair AB13:S15K, where the stations are separated by ~2km, show some difference in signal and lower cross-correlation compared to the co-located stations. An examination of the sites where these stations are deployed revealed that the difference in the spectrograms is likely due to site effects caused by the ~2km offset (Figure S5 in the electronic supplement). Therefore, for the purposes of a study such as this, where we investigate whether co-located GNSS and seismic stations detect comparable ground motion, it is important to select those that have the same location and base. However, based on our results, we infer that seismic and GNSS stations within a given region will contain the same seismic signature in the event of an earthquake. This offers the potential for their joint or interchangeable use in rapid earthquake characterization.

Further, we find that the PGV-derived moment magnitude using GNSS, seismic, and joint data within GNSS frequency bands are well within the uncertainties estimated by Fang et al. (2020). The evolution curves using GNSS data (L1+L2, L2) show clear jumps in the magnitude as contributions from individual stations come in (Figure 4a). The magnitude evolution using strong-motion data also follows a similar trend as the GNSS data with the magnitude evolving at comparable times during the course of the earthquake. However, the final magnitude and smoothness of the curve are limited by the number of relevant strong-motion stations for this event. The joint dataset shows a nearly identical style of magnitude evolution as that of the GNSS data, further pointing to interchangeable/joint use of GNSS and seismic data for rapid characterization of an earthquake.

Another important observation is the difference between the absolute magnitudes of instavel- and seismic-PGVs in the near field. We find that GNSS frequencies exploited in this study do not reflect the near-field high-frequency ground motion (e.g., Grapenthin et al., 2018). This is best illustrated in the co-located GNSS/strong-motion pair AC12 (GNSS) and AK.CHN (strong-motion). Despite their location and similarity in deployment - both located atop a cliff (See Data and Resources) a few meters apart, the total-PGV observed at AK.CHN (5.5 cm/s) is larger than that at AC12 (4.4 cm/s) (Table 1), although the overall cross-correlation of the full signal is good (e.g., East-component cross-correlation = 0.77; lag = -1; Figure S2 in the electronic supplement). This near-field disparity evens out the farther we move from the epicenter, at distances of >200 km. Station pair AC34 (GNSS; total-PGV = 4.4 cm/s) : AK.S19K (strong motion; total-PGV = 4.5 cm/s) (Table 1), co-located at ~300 km from the hypocenter, vividly illustrate the GNSS and seismic PGVs equalizing over larger distances (e.g., East-component cross-correlation = 0.9; lag = -1; Figure 2a). Differences in PGV amplitudes at closely-located stations can also be explained by site effects, as is evident in the case of GNSS station AB13 and strong-motion station AK.S15K (see Figures S3 and S5 in the electronic supplement; Table 1). AB13 is located at the edge of a cliff, while AK.S15K is located ~2km inland from the cliff. It follows that the two time series show lower coherence than those of co-located pairs (e.g., East-component cross-correlation = 0.6; lag = 0; Supplementary Figure S2a). Despite the fact that both stations lie at similar azimuths from the epicenter and are separated by a short distance, near-field and site effects can result in substantially different time series.

This difference in PGV amplitudes with distance is best reflected in the ShakeMaps products (Figure 5; Figure S4 in the electronic supplement). The PGV contours generated using instavels show a slightly narrower band for the 20cm/s excitation (Figure 5a), while the corresponding band in the re-sampled seismic PGVs extends farther in the direction away from the trench (Figure 5b). The near field mismatch between GNSS and seismic PGVs could either be caused by the relatively lower sampling rates in GNSS measurements and/or differences in station deployment (e.g., AB13:S15K). However, GNSS efficiently captures far field motion (>200 km), despite the 1Hz data failing to capture the high frequency content that remains focused in the near field and attenuates with distance (e.g., Grapenthin et al., 2018). The co-/closely-located GNSS and strong-motion PGVs result in nearly identical ground motion contours, except for small variations in the near-field as stated previously (Figure 5a,b). Similarly, when the three GNSS stations in Figure 5c are substituted with corresponding co-/closely located strong-motion stations, we find that the resultant PGV contour output is largely unaltered (Figure 5d). This test using co-/closely-located GNSS and strong-motion stations clearly illustrates that similarly sampled and processed GNSS and seismic data result in comparable ground motion estimates. Therefore, continuing work is focused on how best to leverage these data for use in products such as the ShakeMap.

While GNSS is capable of characterizing the earthquake comparably to that from seismic records, their current operational sampling rates are at least an order or two smaller than their seismic counterparts. Globally, GNSS receivers largely sample at 1 Hz, although there is a systematic growth towards employing 5Hz and 10Hz sampling receivers, mainly limited by telemetry considerations. At reasonable distances away from areas of high energy (frequency) release, employing GNSS-derived PGVs for earthquake rapid estimation is useful and easy to implement, since it is readily adaptable to work on real-time data streams and requires only short-term stable station monumentation, making it useful for rapid, large-scale deployments. The resulting velocities could be integrated into source modeling algorithms, which could prove useful in regions that have limited seismic coverage. Similarly, the instavel rapid characterization approach can be applied to seismic data in regions where there is readily available, functional seismic network even if there is a dearth of GNSS deployments. Therefore, PGVs derived from GNSS and seismic devices are capable of substituting one another and/or working in tandem, depending on data availability and sampling, and could also be used jointly as illustrated in our study.

Conclusions

This study in the context of the 2021 Mw 8.2 Chignik earthquake illustrates that for this earthquake, co-located seismic and GNSS records are quite similar to one another. This demonstrates the potential to use them as interchangeable datasets, or in combination for ground motion estimation (for instance, in ShakeMaps). We employed 1Hz GNSS and re-sampled seismic data to identify the 2021 Mw 8.2 Chignik earthquake within the frequency range of 0.001-0.25 Hz. Peak ground velocities, PGVs, obtained using 1Hz GNSS and seismic data were used to generate rapid estimates of PGV-derived moment magnitudes for the earthquake. We find that the estimates from GNSS and joint GNSS/seismic data result in values within ~±0.4 magnitude units of the final magnitude of Mw 8.2. This agrees with PGV, hypocentral distance, and moment magnitude scaling relationship prescribed by Fang et al. (2020). The PGVs derived from seismic data slightly underestimate the moment magnitude, although this could be attributed to the scaling relationships that were defined primarily using GNSS data.

Meanwhile, ShakeMaps generated using the GNSS and seismic PGVs provide important insights into the conditions under which GNSS could be used as an alternative to or jointly with seismic data. We observe that, in the case of the 2021 Chignik earthquake, GNSS and seismic PGVs are nearly identical when near-field, co-/closely-located GNSS and strong-motion stations are employed. We also note that, substituting co-located GNSS and seismic stations with another introduces negligible changes in the extents of the PGV contours. However, GNSS underestimates near-field ground motion compared to neighboring seismic stations at distances <200 km from the epicenter. We believe that this is a direct consequence of differences in sampling rates between the 1Hz GNSS receiver and the 50Hz or 100Hz seismic station. It is likely that the GNSS receiver, operating at a lower sampling rate, fails to record larger ground motion at higher frequencies. Therefore, the first step to incorporating GNSS data into ShakeMap generation would be to mitigate for differences in observations due to sampling mismatch.

Data and Resources

Seismograms and related metadata used in this study were obtained from the Alaska Earthquake Center (doi.org/10.7914/SN/AK). The facilities of IRIS Data Services (https://service.iris.edu), and specifically the IRIS Data Management Center, were used for access to these waveforms, related metadata, and/or derived products used in this study. The GNSS data used here can be procured from University NAVSTAR Consortium (UNAVCO) at unavco.org, and the associated references are cited in this manuscript. The codes used are cited in the manuscript. Additional information to this manuscript can be found in the electronic supplement. Station specific data for GPS and seismic stations were obtained from https://www.unavco.org/instrumentation/ and https://earthquake.alaska.edu/network respectively.

Acknowledgments

RP and RG were supported through NASA ESI #80NSSC20K0761. MW and AF supported by the Office of State Seismologist of Alaska. This material is based on services provided by the GAGE Facility, operated by UNAVCO, Inc., with support from the National Science Foundation, the National Aeronautics and Space Administration, and the U.S. Geological Survey under NSF Cooperative Agreement EAR-1724794. IRIS Data Services are funded through the Seismological Facilities for the Advancement of Geoscience (SAGE) Award of the National Science Foundation under Cooperative Support Agreement EAR-1851048. Seismic data were recorded by the Alaska Earthquake Center under support from the USGS ANSS program cooperative agreement #G22AC00001 and retrieved via IRIS Web Services. IRIS Data Services are funded through the Seismological Facilities for the Advancement of Geoscience (SAGE) Award of the National Science Foundation under Cooperative Support Agreement EAR-1851048.

References

Aster, R. C., B. Borchers, and C. H. Thurber (2018). Parameter Estimation and Inverse Problems, Second Ed., Elsevier Academic Press, Amsterdam, The Netherlands, 360 pp.

Benedetti, E., M. Branzanti, L. Biagi, G. Colosimo, A. Mazzoni, and M. Crespi (2014). Global Navigation Satellite Systems seismology for the 2012 M w 6.1 Emilia earthquake: Exploiting the VADASE algorithm, Seismol. Res. Lett. 85, no. 3, 649–656.

Benz, H.M., Herman, M., Tarr, A.C., Hayes, G.P., Furlong, K.P., Villaseñor, A., Dart, R.L. and Rhea, S., (2011). *Seismicity of the Earth 1900-2010 Aleutian arc and vicinity* (No. 2010-1083-B). US Geological Survey.

Beyreuther, M., Barsch, R., Krischer, L., Megies, T., Behr, Y. and Wassermann, J., (2010). ObsPy: A Python toolbox for seismology. *Seismological Research Letters*, *81*(3), pp.530-533.

Bock, Y., D. Melgar, and B. W. Crowell (2011). Real-time strong-motion broadband displacements from collocated GPS and accelerometers, Bull. Seismol. Soc. Am. 101, no. 6, 2904–2925, doi: 10.1785/ 0120110007.

Colosimo, G., M. Crespi, and A. Mazzoni (2011). Real-time GPS seismology with a stand-alone receiver: A preliminary feasibility demonstration, J. Geophys. Res. 116, no. 11, 1–14, doi: 10.1029/ 2010JB007941.

Cross, R.S. and Freymueller, J.T., 2008. Evidence for and implications of a Bering plate based on geodetic measurements from the Aleutians and western Alaska. *Journal of Geophysical Research: Solid Earth*, *113*(B7).

Crowell, B. W., D. Melgar, Y. Bock, J. S. Haase, and J. Geng (2013), Earthquake magnitude scaling using seismogeodetic data, Geophys. Res. Lett., 40, 6089–6094, doi:10.1002/2013GL058391.

Crowell, B.W. and Melgar, D., 2020. Slipping the Shumagin gap: A kinematic coseismic and early afterslip model of the Mw 7.8 Simeonof Island, Alaska, earthquake. *Geophysical Research Letters*, *47*(19), p.e2020GL090308.

Crowell, B. W., D. A. Schmidt, P. Bodin, J. E. Vidale, J. Gomberg, J. R. Hartog, V. C. Kress, T. I. Melbourne, M. Santillan, S. E. Minson, et al. (2016). Demonstration of the Cascadia G-FAST geodetic earthquake early warning system for the Nisqually, Washington, earthquake Seismol. Res. Lett. 87, no. 4, doi: 10.1785/0220150255.

Davies, J., Sykes, L., House, L. and Jacob, K., (1981). Shumagin seismic gap, Alaska Peninsula: History of great earthquakes, tectonic setting, and evidence for high seismic potential. *Journal of Geophysical Research: Solid Earth*, *86*(B5), pp.3821-3855.

Drooff, C. and Freymueller, J.T., (2021). New constraints on slip deficit on the Aleutian megathrust and inflation at Mt. Veniaminof, Alaska from repeat GPS measurements. *Geophysical Research Letters*, *48*(4), p.e2020GL091787.

Elliott, J.L., Grapenthin, R., Parameswaran, R.M., Xiao, Z., Freymueller, J.T. and Fusso, L., (2022). Cascading rupture of a megathrust. *Science advances*, *8*(18), p.eabm4131.

Fang, R., Zheng, J., Geng, J., Shu, Y., Shi, C. and Liu, J., (2020). Earthquake magnitude scaling using peak ground velocity derived from high- rate GNSS observations. *Seismological Society of America*, *92*(1), pp.227-237.

Fournier, T.J. and Freymueller, J.T., (2007). Transition from locked to creeping subduction in the Shumagin region, Alaska. *Geophysical Research Letters*, *34*(6).

Freymueller, J.T., Woodard, H., Cohen, S.C., Cross, R., Elliott, J., Larsen, C.F., Hreinsdottir, S., Zweck, C., Haeussler, P.J., Wesson, R. and Ekström, G., (2008). Active deformation processes in Alaska, based on 15 years of GPS measurements. *Active tectonics and seismic potential of Alaska*, *179*, pp.1-42.

Hongcai, Z., Melgar, D. and Goldberg, D.E., (2021). Magnitude calculation without saturation from strong- motion waveforms. *Bulletin of the Seismological Society of America*, *111*(1), pp.50-60.

Gaglione, S. (2015). How does a GNSS receiver estimate velocity?, Inside GNSS (March/April), 38–41.

Given, D. D., E. S. Cochran, T. H. Heaton, E. Hauksson, R. M. Allen, M. Hellweg, J. Vidale, and P. Bodin (2014). Technical implemen- tation plan for the ShakeAlert production system: An earthquake early warning system for the West Coast of the United States, U.S. Geol. Surv. Open-File Rept. 2014-1097, 25 pp., doi: 10.3133/ ofr20141097.

Grapenthin, R., I. A. Johanson, and R. M. Allen (2014a). Operational real-time GPS enhanced earthquake early warning, J. Geophys. Res. 119, no. 10, 7944–7965, doi: 10.1002/2014JB011400.

Grapenthin, R., I. A. Johanson, and R. M. Allen (2014b). The 2014 Mw 6.0 Napa earthquake, California: Observations from real-time GPS-enhanced earthquake early warning, Geophys. Res. Lett. 41, no. 23, 8269–8276, doi: 10.1002/2014GL061923.

Grapenthin, R., M. West, and J. Freymueller (2017). The utility of GNSS for earthquake early warning in regions with sparse seismic networks, Bull. Seismol. Soc. Am. 107, no. 4, 1883–1890.

Grapenthin, R., West, M., Tape, C., Gardine, M. and Freymueller, J., (2018). Single-frequency instantaneous GNSS velocities resolve dynamic ground motion of the 2016 Mw 7.1 Iniskin, Alaska, earthquake. *Seismological Research Letters*, *89*(3), pp.1040-1048.

Ichinose, G., Somerville, P., Thio, H.K., Graves, R. and O'Connell, D., (2007). Rupture process of the 1964 Prince William Sound, Alaska, earthquake from the combined inversion of seismic, tsunami, and geodetic data. *Journal of Geophysical Research: Solid Earth*, *112*(B7).

Johnson, J.M. and Satake, K., (1994). Rupture extent of the 1938 Alaskan earthquake as inferred from tsunami waveforms. *Geophysical Research Letters*, *21*(8), pp.733-736.

Koketsu, K., Miyake, H., Fujiwara, H. and Hashimoto, T., (2008), October. Progress towards a Japan integrated velocity structure model and long-period ground motion hazard map. In Proceedings of the 14th World conference on earthquake engineering (pp. S10-038). Beijing: China Seismological Society.

Krischer, L., Fichtner, A., Zukauskaite, S. and Igel, H., (2015). Large- scale seismic inversion framework. *Seismological Research Letters*, *86*(4), pp.1198-1207.

Kuyuk, H.S., Allen, R.M., Brown, H., Hellweg, M., Henson, I. and Neuhauser, D., (2014). Designing a network- based earthquake early warning algorithm for California: ElarmS- 2. *Bulletin of the Seismological Society of America*, *104*(1), pp.162-173.

Lewandowski, W. and Arias, E.F., 2011. GNSS times and UTC. *Metrologia*, *48*(4), p.S219. doi:10.1088/0026-1394/48/4/S14

Liu, C., Lay, T. and Xiong, X., (2022). The 29 July 2021 MW 8.2 Chignik, Alaska Peninsula Earthquake Rupture Inferred From Seismic and Geodetic Observations: Re-Rupture of the Western 2/3 of the 1938 Rupture Zone. *Geophysical Research Letters*, *49*(4), p.e2021GL096004.

López, A.M. and Okal, E.A., (2006). A seismological reassessment of the source of the 1946 Aleutian 'tsunami' earthquake. *Geophysical Journal International*, *165*(3), pp.835-849.

Megies, T., Beyreuther, M., Barsch, R., Krischer, L. and Wassermann, J., (2011). ObsPy–What can it do for data centers and observatories?. *Annals of Geophysics*, *54*(1), pp.47-58.

Melgar, D., R. M. Allen, S. Riquelme, J. Geng, F. Bravo, J. C. Baez, H. Parra, S. Barrientos, P. Fang, Y. Bock, et al. (2016). Local tsunami warnings: Perspectives from recent large events, Geophys. Res. Lett. 43, no. 3, 1109–1117, doi: 10.1002/2015GL067100.

Misra, P., and P. Enge (2011). Global Positioning System: Signals, Measure- ments and Performance, Second Ed., Ganga-Jamuna Press, 569 pp.

Morikawa, N. and Fujiwara, H., (2013). A new ground motion prediction equation for Japan applicable up to M9 mega-earthquake. Journal of Disaster Research, 8(5), pp.878-888.

Rinehart, A.J., McKenna, S.A. and Dewers, T.A., 2016. Using wavelet covariance models for simultaneous picking of overlapping P- and S- wave arrival times in noisy single- component data. *Seismological Research Letters*, *87*(4), pp.893-900.

Stauder, W., (1968). Mechanism of the Rat Island earthquake sequence of February 4, 1965, with relation to island arcs and sea- floor spreading. *Journal of Geophysical Research*, *73*(12), pp.3847-3858.

Sykes, L.R., Kisslinger, J.B., House, L., Davies, J.N. and Jacob, K.H., 1981. Rupture zones and repeat times of great earthquakes along the Alaska- Aleutian arc, 1784–1980. *Earthquake Prediction: An International Review*, *4*, pp.73-80.

UNAVCO Community, (2004), PBO GPS Network - AB07-SandPoint_AK2004 P.S., UNAVCO, GPS/GNSS Observations Dataset, https://doi.org/10.7283/T59W0CDH

UNAVCO Community, 2004, PBO GPS Network - AC27-AC27MNeil_AK2004 P.S., UNAVCO, GPS/GNSS Observations Dataset, https://doi.org/10.7283/T5PR7T1N

UNAVCO Community, 2005, PBO GPS Network - AC25-King_Cove_AK2005 P.S., UNAVCO, GPS/GNSS Observations Dataset, https://doi.org/10.7283/T5SF2T4X

UNAVCO Community, (2006), PBO GPS Network - AB13-ChignikLgnAK2006 P.S., UNAVCO, GPS/GNSS Observations Dataset, https://doi.org/10.7283/T5HQ3WW8

UNAVCO Community, 2006, PBO GPS Network - AC02-AkhiokCorpAK2005 P.S., UNAVCO, GPS/GNSS Observations Dataset, https://doi.org/10.7283/T5Z60M01

UNAVCO Community, (2006), PBO GPS Network - AC21-PerryvilleAK2006 P.S., UNAVCO, GPS/GNSS Observations Dataset, https://doi.org/10.7283/T5KK98RJ

UNAVCO Community, 2006, PBO GPS Network - AC34-OldHarbor_AK2006 P.S., UNAVCO, GPS/GNSS Observations Dataset, https://doi.org/10.7283/T5028PG3

UNAVCO Community, 2006, PBO GPS Network - AC39-ShuyakIsSPAK2006 P.S., UNAVCO, GPS/GNSS Observations Dataset, https://doi.org/10.7283/T5TT4NX1

UNAVCO Community, (2006), PBO GPS Network - AC41-PortMollerAK2006 P.S., UNAVCO, GPS/GNSS Observations Dataset, https://doi.org/10.7283/T5FX77D3

UNAVCO Community, 2006, PBO GPS Network - AC45-SitkinakIsAK2006 P.S., UNAVCO, GPS/GNSS Observations Dataset, https://doi.org/10.7283/T5JS9NDC

UNAVCO Community, 2006, PBO GPS Network - AC67-PillarMtn_AK2006 P.S., UNAVCO, GPS/GNSS Observations Dataset, https://doi.org/10.7283/T5Q23X61

UNAVCO Community, (2007), PBO GPS Network - AB02-Nikolski__AK2007 P.S., UNAVCO, GPS/GNSS Observations Dataset, https://doi.org/10.7283/T5X63JX4

UNAVCO Community, 2007, PBO GPS Network - AB14-DillinghamAK2007 P.S., UNAVCO, GPS/GNSS Observations Dataset, https://doi.org/10.7283/T5HT2M90

UNAVCO Community, 2007, PBO GPS Network - AC08-CapDouglasAK2007 P.S., UNAVCO, GPS/GNSS Observations Dataset, https://doi.org/10.7283/T5HH6H21

UNAVCO Community, (2007), PBO GPS Network - AC40-PortHeidenAK2007 P.S., UNAVCO, GPS/GNSS Observations Dataset, https://doi.org/10.7283/T50G3H4S

UNAVCO Community, 2007, PBO GPS Network - AC42-SanakIslndAK2007 P.S., UNAVCO, GPS/GNSS Observations Dataset, https://doi.org/10.7283/T5VX0DJ1

UNAVCO Community, 2007, PBO GPS Network - AC47-SlopeMtn__AK2007 P.S., UNAVCO, GPS/GNSS Observations Dataset, https://doi.org/10.7283/T5N58JC1

UNAVCO Community, 2007, PBO GPS Network - AC52-PilotPointAK2007 P.S., UNAVCO, GPS/GNSS Observations Dataset, https://doi.org/10.7283/T5ZP444C

UNAVCO Community, (2008a), PBO GPS Network - AC12-ChernaburaAK2008 P.S., UNAVCO, GPS/GNSS Observations Dataset, https://doi.org/10.7283/T5NV9G7P

UNAVCO Community, (2008b), PBO GPS Network - AC13-ChirikofIsAK2008 P.S., UNAVCO, GPS/GNSS Observations Dataset, https://doi.org/10.7283/T5F18WRV

UNAVCO Community, 2008, PBO GPS Network - AC26-Cape_Gull_AK2008 P.S., UNAVCO, GPS/GNSS Observations Dataset, https://doi.org/10.7283/T58P5XJF

UNAVCO Community, 2008, PBO GPS Network - AC28-NagaiIslndAK2008 P.S., UNAVCO, GPS/GNSS Observations Dataset, https://doi.org/10.7283/T53N21DV

Witter, R.C., Briggs, R.W., Engelhart, S.E., Gelfenbaum, G., Koehler, R.D. and Barnhart, W.D., 2014. Little late Holocene strain accumulation and release on the Aleutian megathrust below the Shumagin Islands, Alaska. *Geophysical Research Letters*, *41*(7), pp.2359-2367.

Worden, C.B., Gerstenberger, M.C., Rhoades, D.A. and Wald, D.J., (2012). Probabilistic relationships between ground- motion parameters and modified Mercalli intensity in California. *Bulletin of the Seismological Society of America*, *102*(1), pp.204-221.

Wu, F.T. and Kanamori, H., (1973). Source mechanism of February 4, 1965, Rat island earthquake. *Journal of Geophysical Research*, *78*(26), pp.6082-6092.

Xiao, Z., Freymueller, J.T., Grapenthin, R., Elliott, J.L., Drooff, C. and Fusso, L., (2021). The deep Shumagin gap filled: Kinematic rupture model and slip budget analysis of the 2020 Mw 7.8 Simeonof earthquake constrained by GNSS, global seismic waveforms, and floating InSAR. *Earth and Planetary Science Letters*, *576*, p.117241.

Ye, L., Lay, T., Kanamori, H., Yamazaki, Y. and Cheung, K.F., (2021). The 22 July 2020 Mw 7.8 Shumagin seismic gap earthquake: Partial rupture of a weakly coupled megathrust. *Earth and Planetary Science Letters*, *562*, p.116879.

Ye, L., Bai, Y., Si, D., Lay, T., Cheung, K.F. and Kanamori, H., (2022). Rupture Model for the 29 July 2021 MW 8.2 Chignik, Alaska Earthquake Constrained by Seismic, Geodetic, and Tsunami Observations. *Journal of Geophysical Research: Solid Earth*, p.e2021JB023676.

Mailing addresses

Revathy M. Parameswaran, Ronni Grapenthin, Michael E. West, and Alexander Fozkos

2156 Koyukuk Drive

PO Box 757320

University of Alaska Fairbanks

Fairbanks, AK 99775

Figures Captions

Figure 1: Seismic and GNSS station coverage for the 2021 Mw 8.2 Chignik earthquake. The limits for the 1964 M9.2 Prince William Sound, 1938 M8.3 Semidi, 1946 M7.4 Sanak (or Unimak), and the 1948 M7.9 Shumagin earthquakes are based on Davies et al. (1981). The 0.5m slip contours for the 2020 Mw 7.8 Simeonof earthquake are based on Xiao et al. (2021), and the 1m slip-contours for the 2021 Mw 8.2 Chignik earthquake

are as estimated by Elliott et al. (2022). This study analyzed data from 22 GNSS and 3 strong-motion stations (AK.CHN, AK.S15K, and AK.S19K). Figure also shows some of the other broadband stations in the vicinity of the earthquake, but are not used in this study due to amplitude saturation.

Figure 2: Co-located GNSS vs Strong-motion station pair for the 2021 Chignik earthquake. [a] – [Top] Re-sampled (100 Hz to 1 Hz) and unfiltered east seismic velocity time series from strong-motion station AK.S19K; [Middle] unfiltered east instavel trace from GNSS station AC34; and [Bottom] time series of GNSS noise obtained by differencing the GNSS and the seismic velocity time series. [b] – [Top] Spectrogram of strong-motion derived velocity from AK.S19K; [Middle] Spectrogram of AC34 instavel; and [c] Spectrogram of subtracted time series. The orange box in the bottom panel in [b] highlights the frequency range in which the two signals show strong coherence. This is the band used for the frequency filter.

Figure 3: Cross-correlations for east, north, and vertical components for AC34:S19K. [a] East component - [Top] AK.S19K filtered using Butterworth bandpass 0.001-0.25Hz. [Middle] filtered time series for AC34. [Bottom] Cross-correlation between filtered AK.S19K and AC34. [b] Filtered north components of AK.S19K and AC34, and their cross-correlation. [c] Filtered vertical components of AK.S19K and AC34, and their cross-correlation.

Figure 4: PGV-inferred moment magnitudes and scaling relationships: [a] Evolution of PGV-inferred moment magnitudes with net moment release associated with the 2021 Mw 8.2 Chignik earthquake. PGV-inferred moment magnitudes from GNSS (L2) = 8.06; GNSS (L1+L2) = 7.97; strong-motion = 7.78; joint = 7.9. The gray area marked by the curves indicates the moment release associated with the Chignik earthquake over time (from USGS) [b] PGV vs hypocentral distance plot scaled with corresponding moment magnitudes from 22 GNSS receivers and 3 strong-motion stations. Thick oblique lines are the predicted magnitudes as a function of PGVs and hypocentral distance based on Fang et al. (2020), while the dashed lines are the limits of the same.

Figure 5: PGV contour estimates from the 2021 Mw 8.2 Chignik earthquake from different data sources: [a] PGV contours (dashed and solid colored lines) based on instavels from GNSS stations (AB13, AC12, AC34). [b] Contours using velocity data from the 3 corresponding co-/closely-located strong-motion stations (AK.S15K, AK.CHN, AK.S19K). [c] PGV contours using 22 instavels that were employed for rapid magnitude estimation for the 2021 Chignik earthquake. [d] PGV contours based on 22 GNSS locations with 3 of them replaced by corresponding co-/closely located strong-motion stations. The numbers indicated inside the white boxes on the contours indicate the PGVs in cm/s. Triangles = GNSS stations. Squares = strong-motion stations. Red star = the 2021 Chignik epicenter. Black rectangle shows the bounds of the fault plane.

Table 1: GNSS and seismic PGVs

Hypocentral Distance (km)	GNSS station	Latitude (N)	Longitude (E)	PGV-total (cm/s)	PGV-horizontal (cm/s)
109.6	AC21	55.921	-159.128	8.0	5.8
121.32	AB13	56.307	-158.504	8.5	8.1
128.58	AC12	54.831	-159.590	4.4	3.0
146.82	AC28	55.078	-160.049	5.0	3.3
153.88	AC13	55.822	-155.622	23.7	20.6
170.35	AB07	55.349	-160.477	5.1	4.9
177.2	AC41	55.909	-160.407	8.8	6.9

187.92	AC40	56.930	-158.619	17.9	17.9
252.28	AC52	57.567	-157.574	7.9	6.8
268.98	AC45	56.564	-154.181	7.2	6.8
287.74	AC25	55.089	-162.314	3.6	2.5
292.37	AC02	56.951	-154.183	6.2	4.7
332.5	AC42	54.472	-162.784	4.3	2.0
354.04	AC34	57.220	-153.279	4.4	3.3
394.21	AC26	58.215	-154.150	7.4	3.2
429.22	AB14	59.108	-159.092	4.3	2.2
432.58	AC67	57.791	-152.425	5.6	2.9

475.92	AC08	58.929	-153.645	4.9	2.3
491.29	AC27	59.253	-154.163	6.6	3.3
494.27	AC39	58.610	-152.394	4.5	2.4
614.73	AC47	60.081	-152.624	8.1	3.3
765.57	AB02	52.971	-168.855	4.5	2.0
Hypocentral Distance (km)	**Seismic station**	**Latitude (N)**	**Longitude (E)**	**PGV-total (cm/s)**	**PGV-horizontal (cm/s)**
121.99	**S15K**	56.306	-158.540	10.1	6.9
128.58	**CHN**	54.831	-159.590	5.5	4.6
353.79	**S19K**	57.223	-153.288	4.5	4.3

Figure 1

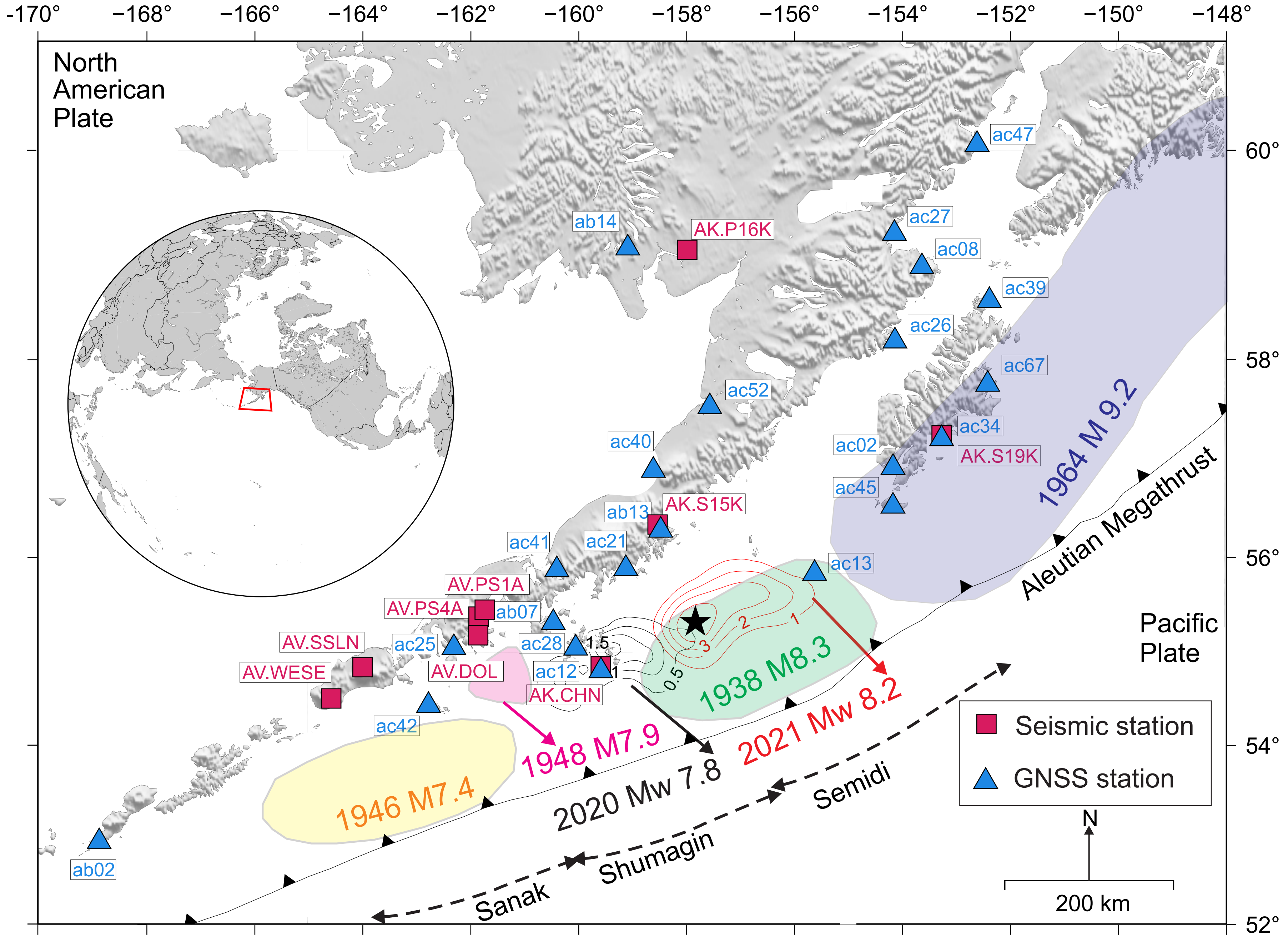

-170°
−168°
−166°
−164°
−162°
−160°
−158°
−156°
−154°
−152°
−150°
−148°
60°
58°
56°
54°
52°
North American Plate
Pacific Plate
ab14
AK.P16K
ac47
ac27
ac08
ac39
ac26
ac67
ac52
ac34
AK.S19K
ac02
ac40
ac45
ab13
AK.S15K
ac41
ac21
ac13
AV.PS1A
AV.PS4A
ab07
AV.SSLN
ac25
ac28
AV.WESE
AV.DOL
ac12
AK.CHN
ac42
ab02
1964 M 9.2
Aleutian Megathrust
1938 M8.3
2021 Mw 8.2
1948 M7.9
2020 Mw 7.8
1946 M7.4
Semidi
Shumagin
Sanak
Seismic station
GNSS station
N
200 km

Figure 2

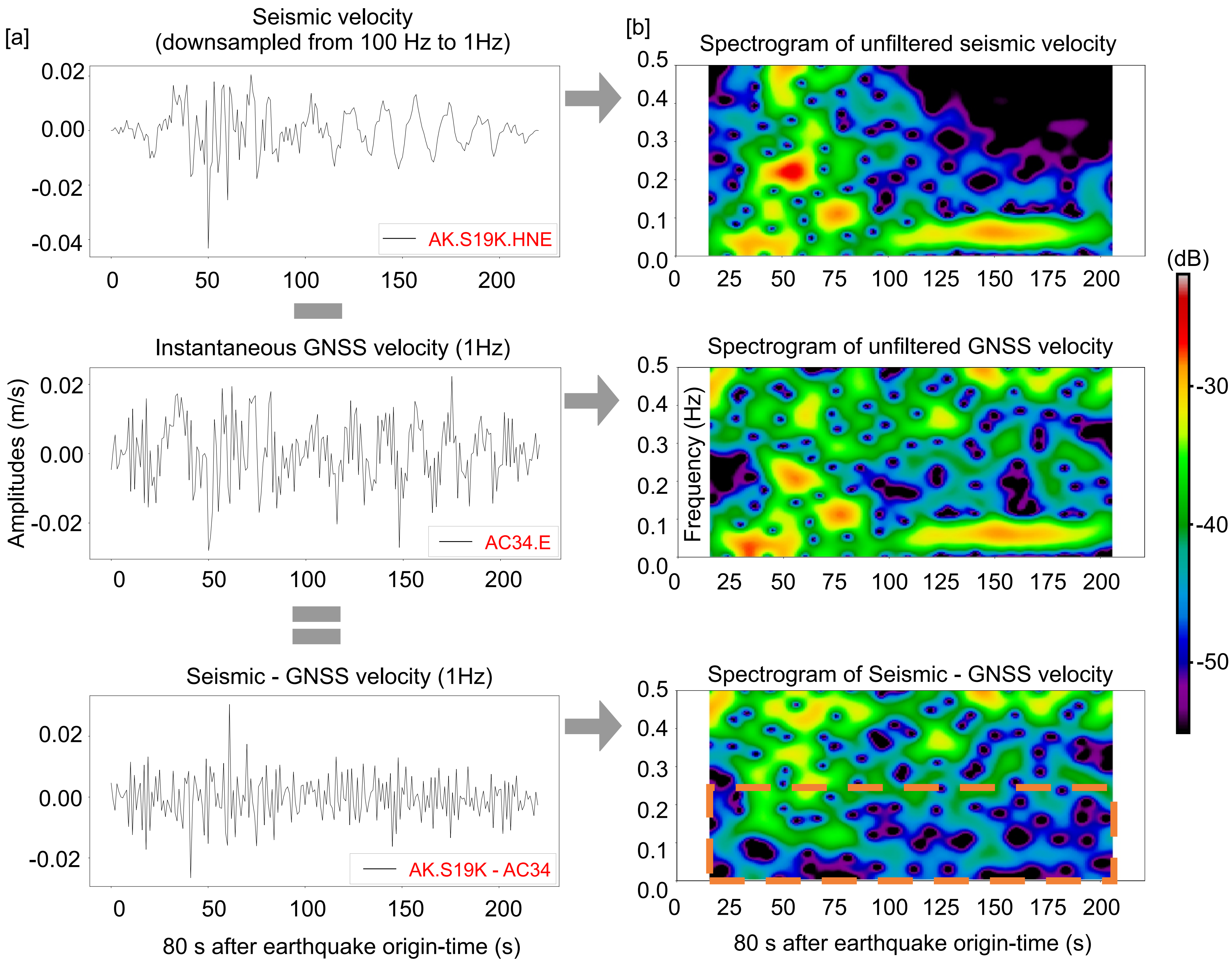
[a]
Seismic velocity
(downsampled from 100 Hz to 1Hz)
AK.S19K.HNE
Instantaneous GNSS velocity (1Hz)
AC34.E
Amplitudes (m/s)
Seismic - GNSS velocity (1Hz)
AK.S19K - AC34
80 s after earthquake origin-time (s)
[b]
Spectrogram of unfiltered seismic velocity
Spectrogram of unfiltered GNSS velocity
Frequency (Hz)
Spectrogram of Seismic - GNSS velocity
80 s after earthquake origin-time (s)
(dB)
-30
-40
-50

Figure 3

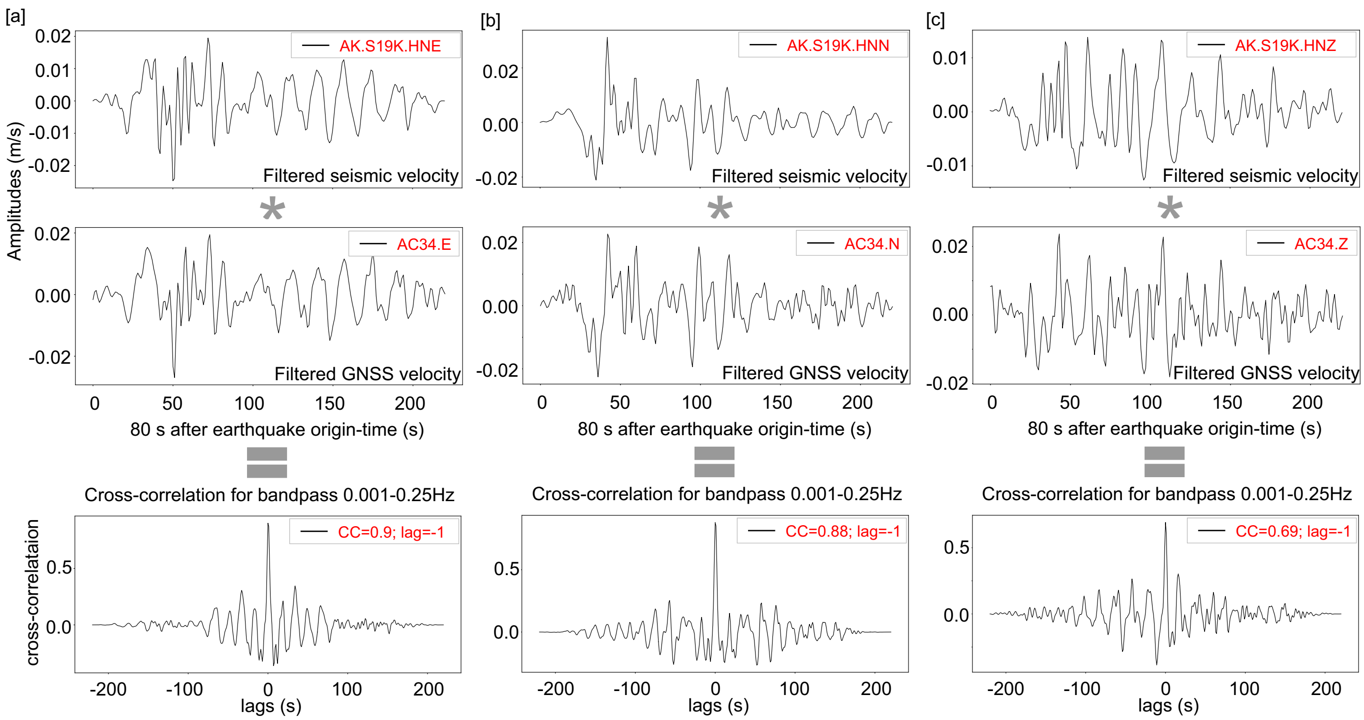
[a]
[b]
[c]
Amplitudes (m/s)
AK.S19K.HNE
AK.S19K.HNN
AK.S19K.HNZ
Filtered seismic velocity
AC34.E
AC34.N
AC34.Z
Filtered GNSS velocity
80 s after earthquake origin-time (s)
Cross-correlation for bandpass 0.001-0.25Hz
cross-correlataion
CC=0.9; lag=-1
CC=0.88; lag=-1
CC=0.69; lag=-1
lags (s)

Figure 4

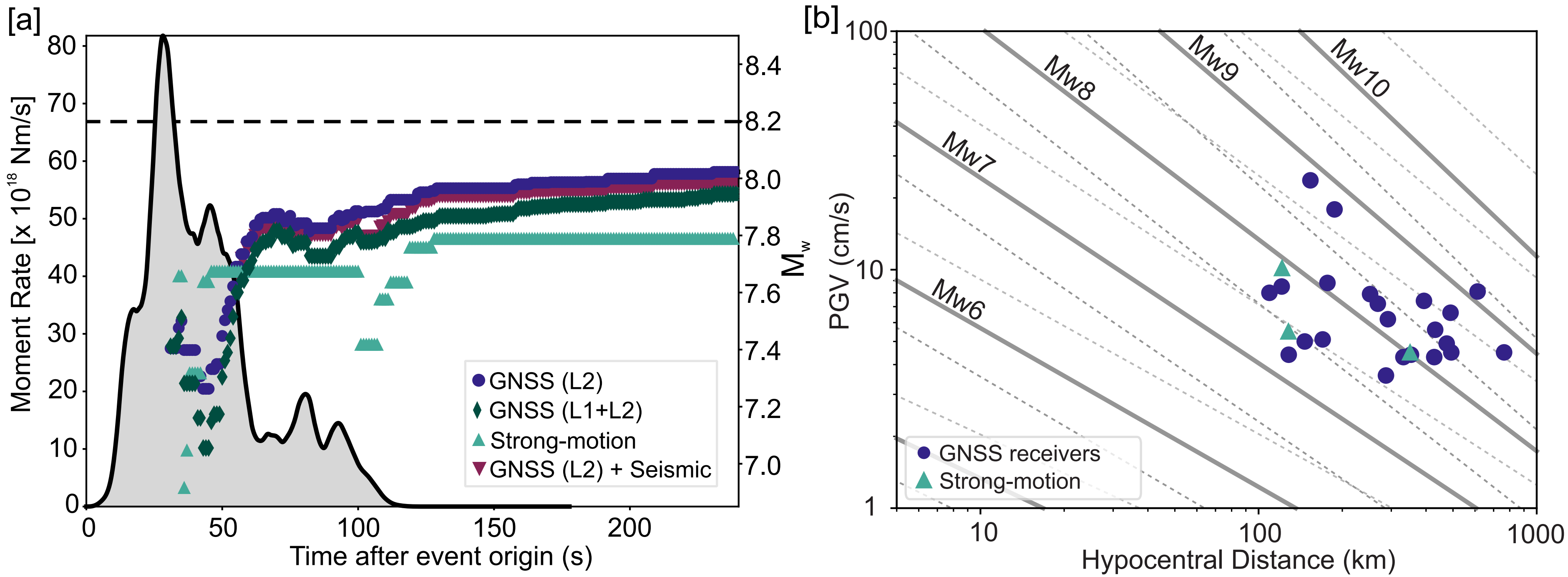
[a]
Moment Rate [x 10^18 Nm/s]
Time after event origin (s)
M_w
GNSS (L2)
GNSS (L1+L2)
Strong-motion
GNSS (L2) + Seismic
[b]
PGV (cm/s)
Hypocentral Distance (km)
Mw6
Mw7
Mw8
Mw9
Mw10
GNSS receivers
Strong-motion

Figure 5

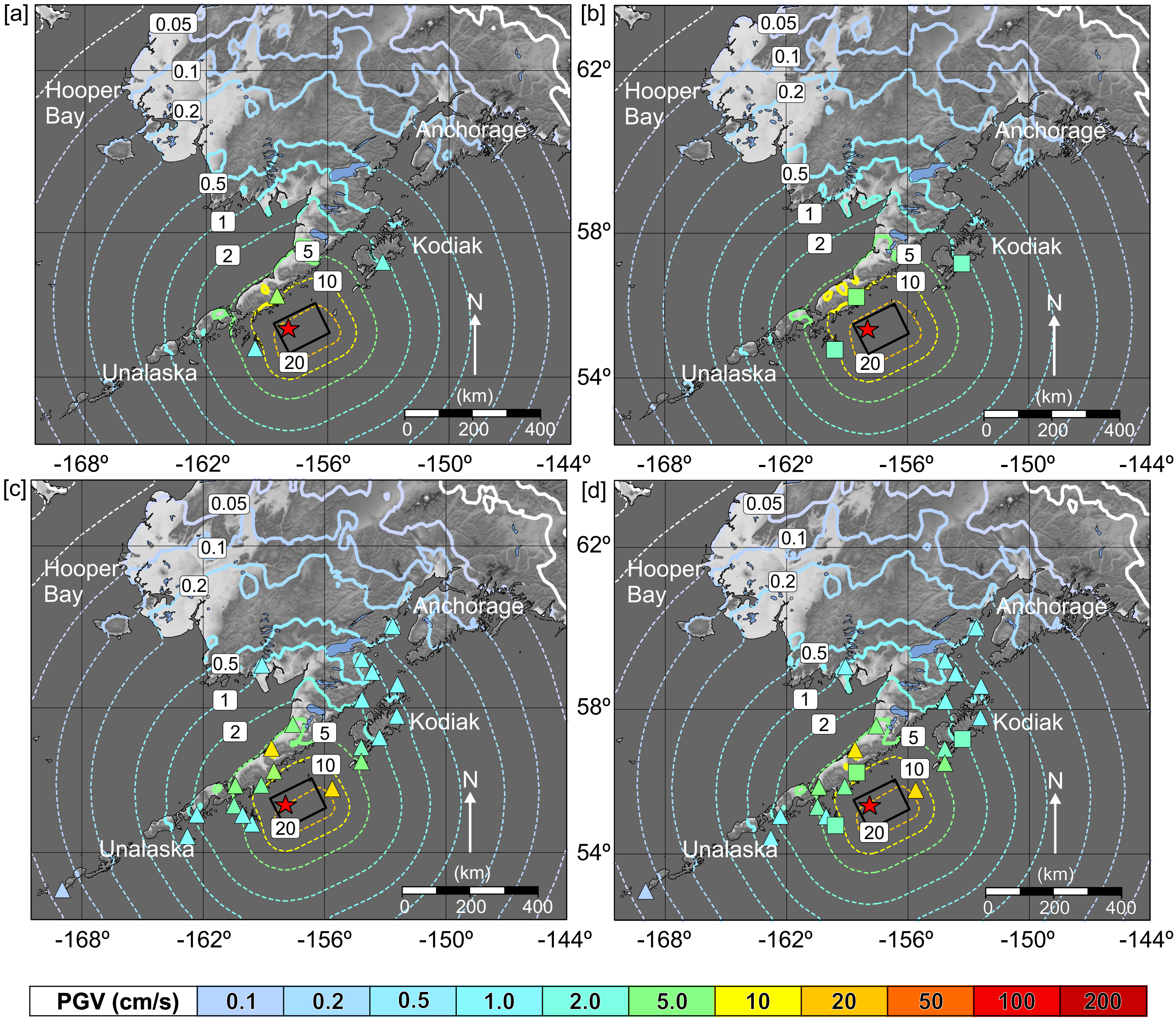
[a]
[b]
[c]
[d]
Hooper Bay
Anchorage
Kodiak
Unalaska
0.05
0.1
0.2
0.5
1
2
5
10
20
N
(km)
0
200
400
62º
58º
54º
-168º
-162º
-156º
-150º
-144º
PGV (cm/s)
0.1
0.2
0.5
1.0
2.0
5.0
10
20
50
100
200

Interchangeable use of GNSS and seismic data for rapid earthquake characterization: 2021 Chignik earthquake, Alaska

Revathy M. Parameswaran[1]*, Ronni Grapenthin[1], Michael West[1], Alex Fozkos[1]

[1]Geophysical Institute, University of Alaska Fairbanks, Fairbanks, AK, 99775

*Corresponding author: rmparameswaran@alaska.edu

Electronic Supplement

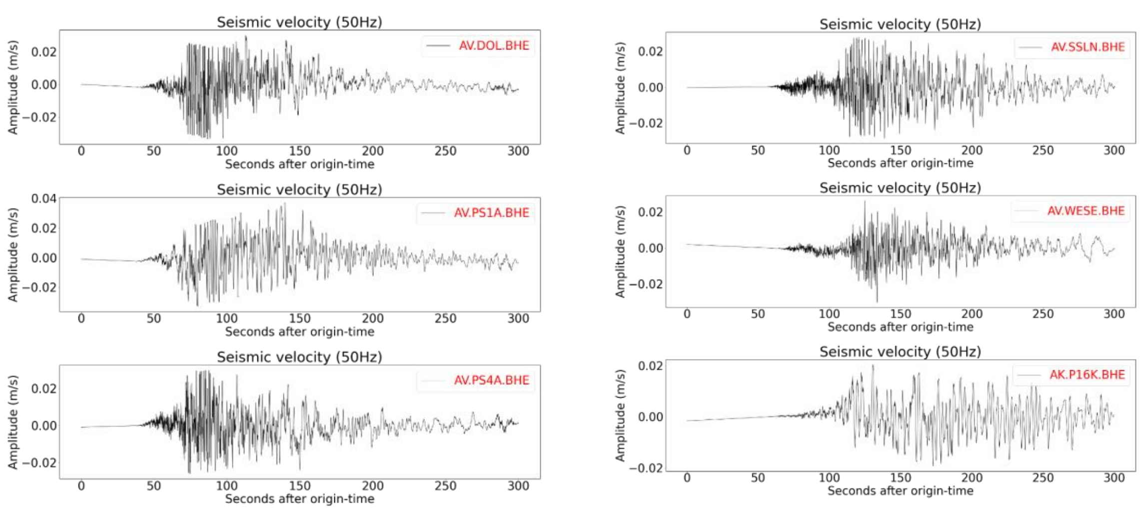

Figure S1: Velocimeter data from the 2021 Chignik earthquake: Instrument-response corrected E-component time-series from 6 of the broadband seismic stations (AV.DOL, AV.PS1A, AV.PS4A, AV.SSLN, AV.WESE, AK.P16K) that were close to and recorded the 2021 Mw 8.2 Chignik earthquake. The station names and channels are indicated in red.

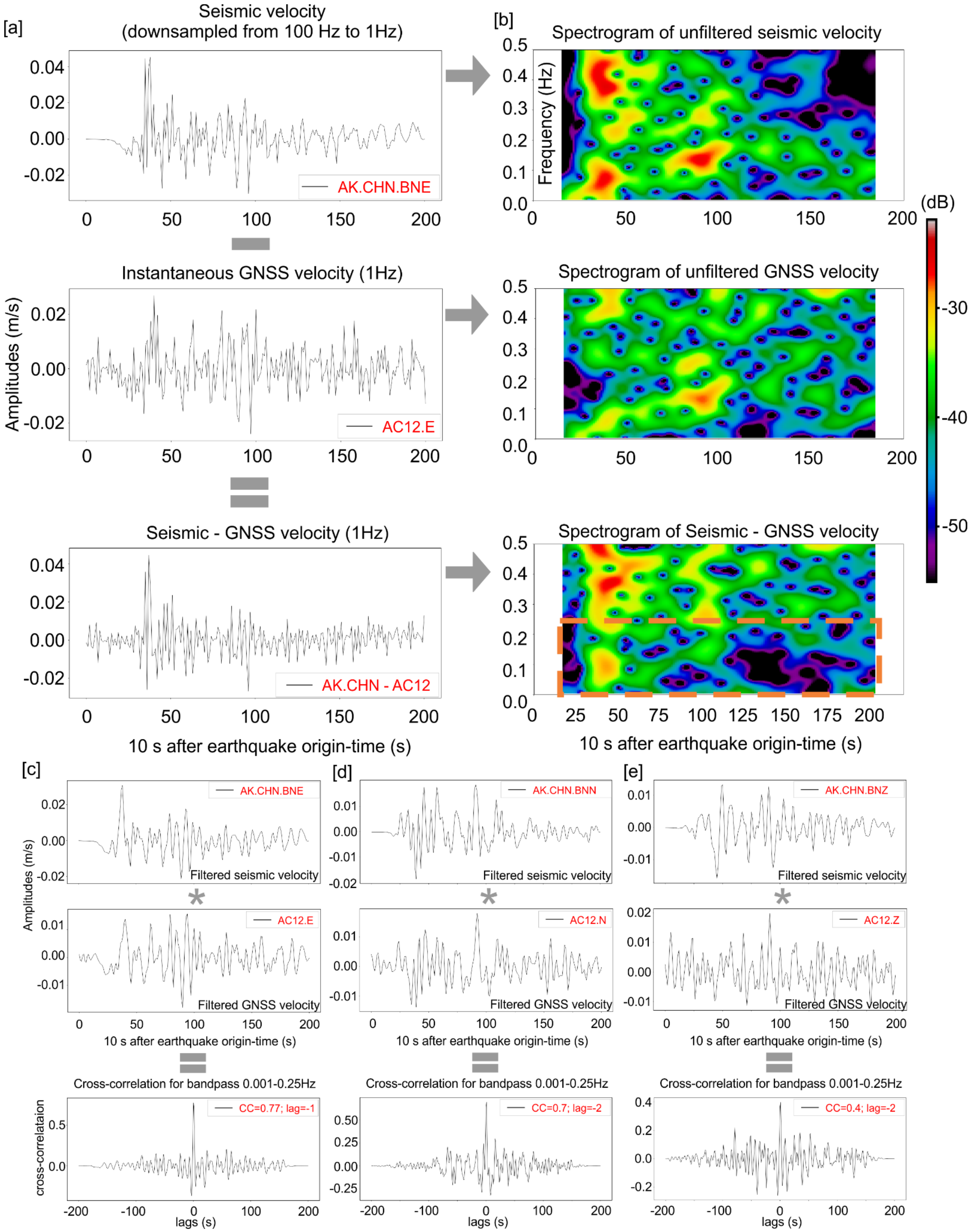
[a]
Seismic velocity
(downsampled from 100 Hz to 1Hz)
AK.CHN.BNE
Instantaneous GNSS velocity (1Hz)
Amplitudes (m/s)
AC12.E
Seismic - GNSS velocity (1Hz)
AK.CHN - AC12
10 s after earthquake origin-time (s)
[b]
Spectrogram of unfiltered seismic velocity
Frequency (Hz)
Spectrogram of unfiltered GNSS velocity
Spectrogram of Seismic - GNSS velocity
10 s after earthquake origin-time (s)
(dB)
[c]
[d]
[e]
AK.CHN.BNE
AK.CHN.BNN
AK.CHN.BNZ
Filtered seismic velocity
AC12.E
AC12.N
AC12.Z
Filtered GNSS velocity
10 s after earthquake origin-time (s)
Cross-correlation for bandpass 0.001-0.25Hz
CC=0.77; lag=-1
CC=0.7; lag=-2
CC=0.4; lag=-2
cross-correlataion
lags (s)

Figure S2: Co-located seismic vs GNSS station pair for the 2021 Chignik earthquake: [a] – [Top] Re-sampled (50 Hz to 1 Hz) and unfiltered seismic velocity time series from strong-motion station AK.CHN; [Middle] unfiltered instavel trace from GNSS station AC12; and [Bottom] time series of GNSS noise obtained by differencing the GNSS and the seismic velocity time series. [b] – [Top] Spectrogram of strong-motion derived velocity from AK.CHN; [Middle] Spectrogram of AC12 instavel; and [Bottom] Spectrogram of subtracted time series. [c] – Filtered velocity time series and cross-correlation; [Top] AK.CHN filtered using butterworth bandpass 0.001-0.25Hz. [Middle] filtered time series for AC12. [Bottom] Cross-correlation between filtered AK.CHN and AC12. The orange box in the bottom panel in [b] highlights the frequency range within which the Chignik earthquake signal is most dominant, and based on which the butterworth filter was defined. [d] Filtered north components of AK.CHN and AC12, and their cross-correlation. [e] Filtered vertical components of AK.CHN and AC12, and their cross-correlation.

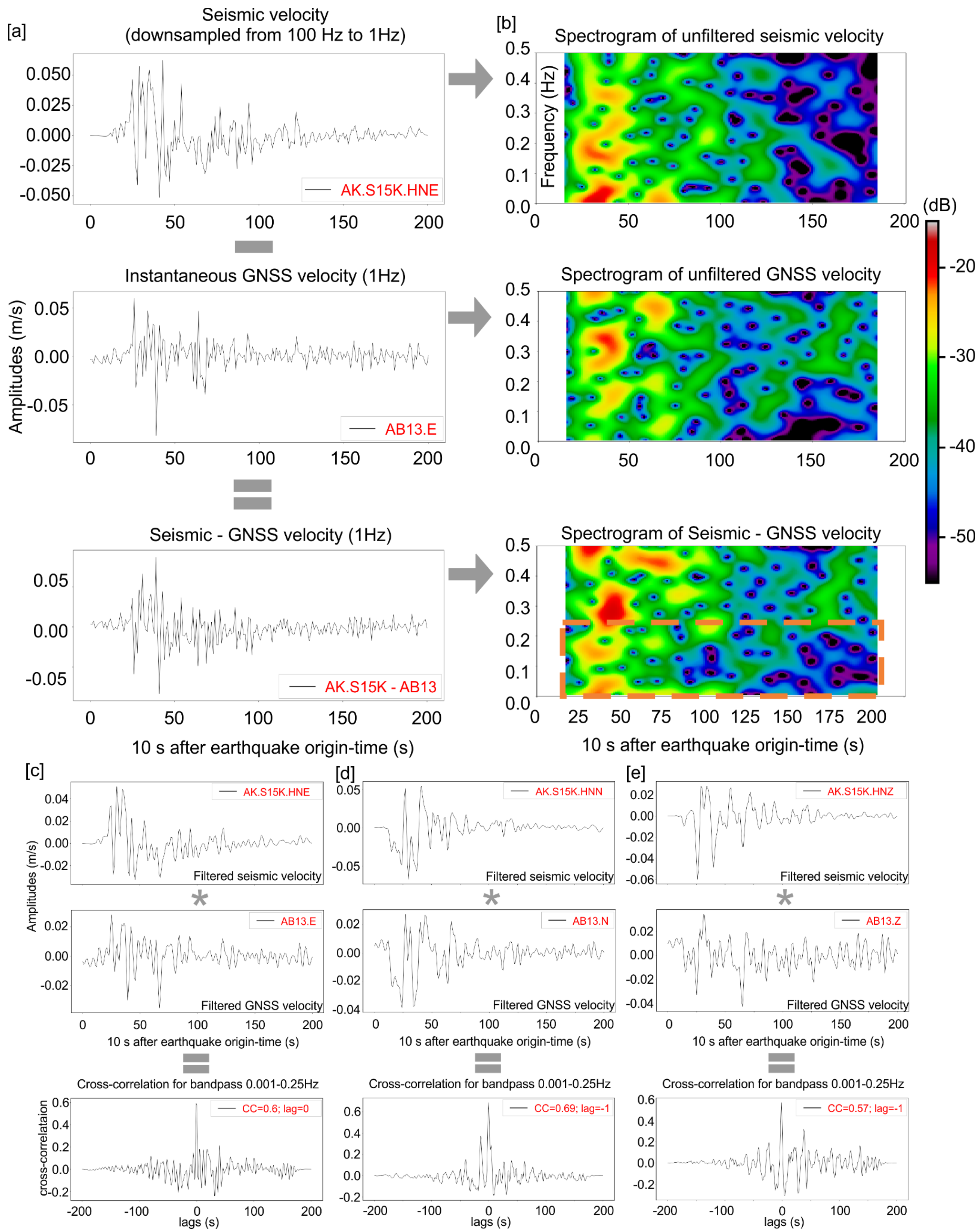
[a]
Seismic velocity
(downsampled from 100 Hz to 1Hz)
AK.S15K.HNE
Instantaneous GNSS velocity (1Hz)
AB13.E
Seismic - GNSS velocity (1Hz)
AK.S15K - AB13
Amplitudes (m/s)
10 s after earthquake origin-time (s)
[b]
Spectrogram of unfiltered seismic velocity
Frequency (Hz)
Spectrogram of unfiltered GNSS velocity
Spectrogram of Seismic - GNSS velocity
10 s after earthquake origin-time (s)
(dB)
[c]
AK.S15K.HNE
Filtered seismic velocity
AB13.E
Filtered GNSS velocity
10 s after earthquake origin-time (s)
Cross-correlation for bandpass 0.001-0.25Hz
CC=0.6; lag=0
cross-correlataion
lags (s)
[d]
AK.S15K.HNN
Filtered seismic velocity
AB13.N
Filtered GNSS velocity
10 s after earthquake origin-time (s)
Cross-correlation for bandpass 0.001-0.25Hz
CC=0.69; lag=-1
lags (s)
[e]
AK.S15K.HNZ
Filtered seismic velocity
AB13.Z
Filtered GNSS velocity
10 s after earthquake origin-time (s)
Cross-correlation for bandpass 0.001-0.25Hz
CC=0.57; lag=-1
lags (s)

29

Figure S3: Closely located seismic vs GNSS station pair for the 2021 Chignik earthquake: [a] – [Top] Re-sampled (100 Hz to 1 Hz) and unfiltered seismic velocity time series from strong-motion station AK.S15K; [Middle] unfiltered instavel trace from GNSS station AB13; and [Bottom] time series of GNSS noise obtained by differencing the GNSS and the seismic velocity time series. [b] – [Top] Spectrogram of strong-motion derived velocity from AK.S15K; [Middle] Spectrogram of AB13 instavel; and [Bottom] Spectrogram of subtracted time series. [c] – Filtered velocity time series and cross-correlation; [Top] AK.S15K filtered using butterworth bandpass 0.001-0.25Hz. [Middle] filtered time series for AB13. [Bottom] Cross-correlation between filtered AK.S15K and AB13. The orange box in the bottom panel in [b] highlights the frequency range within which the Chignik earthquake signal is most dominant, and based on which the butterworth filter was defined. [d] Filtered north components of AK.S15K and AB13, and their cross-correlation. [e] Filtered vertical components of AK.S15K and AB13, and their cross-correlation.

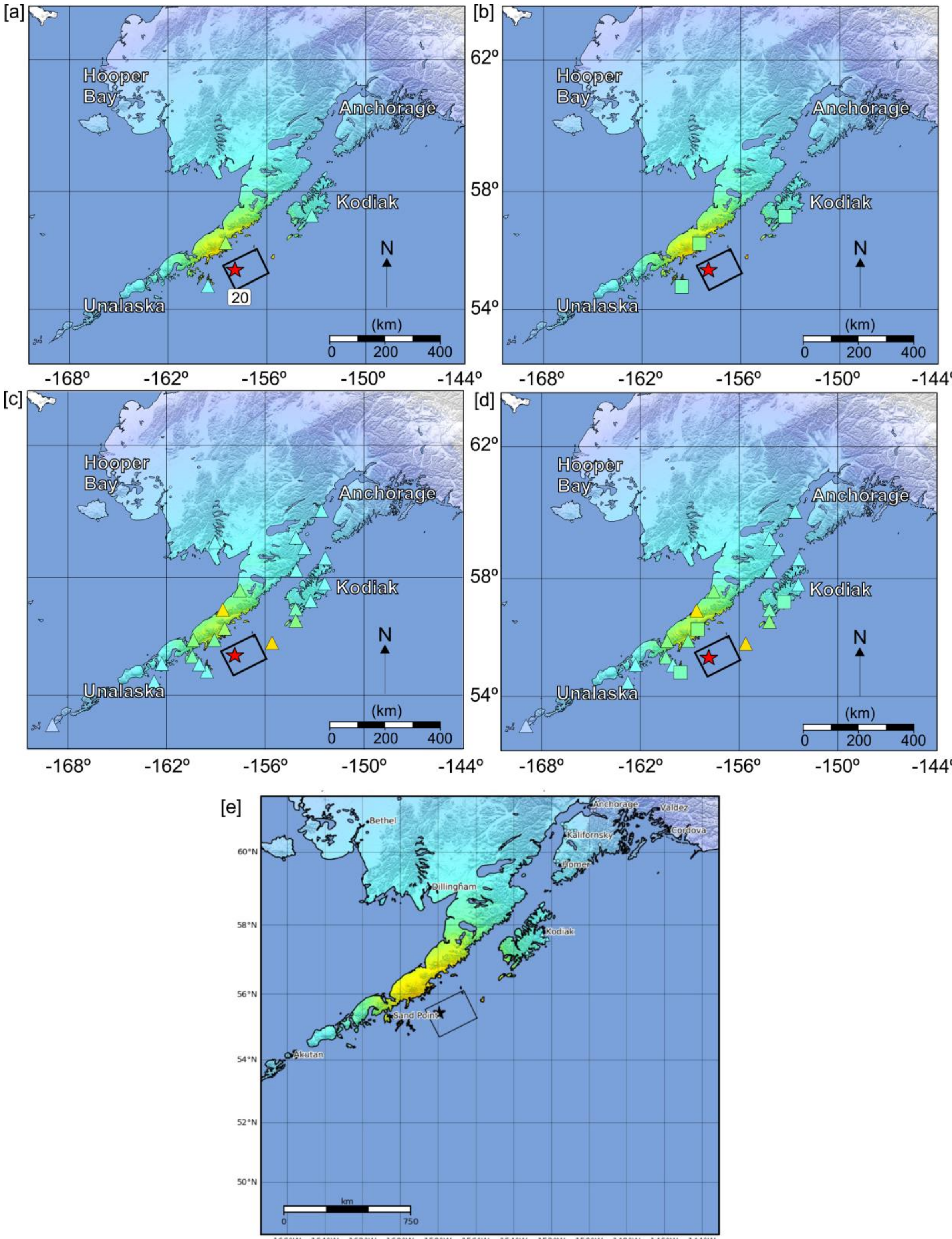

SHAKING	Not felt	Weak	Light	Moderate	Strong	Very Strong	Severe	Violent	Extreme
DAMAGE	None	None	None	Very light	Light	Moderate	Moderate/heavy	Heavy	Very heavy
PGA(%g)	<0.0464	0.297	2.76	6.2	11.5	21.5	40.1	74.7	>139
PGV(cm/s)	<0.0215	0.135	1.41	4.65	9.64	20.0	41.4	85.8	>178
INTENSITY	I	II-III	IV	V	VI	VII	VIII	IX	X+

Figure S4: ShakeMaps for the 2021 Mw 8.2 Chignik earthquake from different data sources: ShakeMaps [a] based on instavels from GNSS stations (AB13, AC12, AC34), and [b] using velocity data from the 3 corresponding co-/closely-located strong-motion stations (AK.S15K, AK.CHN, AK.S19K). ShakeMaps [c] using 22 instavels that were employed for rapid magnitude estimation for the 2021 Chignik earthquake, [d] based on 22 GNSS locations with 3 of them replaced by corresponding co-/closely located strong-motion stations, and [e] officially distributed by USGS (https://earthquake.usgs.gov/product/shakemap/us6000f02w/us/1628043466060/download/intensity.jpg). Triangles = GNSS stations. Squares = strong-motion stations. Triangles in [e] are seismic stations used by the USGS ShakeMap. Red star = the 2021 Chignik epicenter. Black rectangle shows the bounds of the fault plane. The scaling and color-scheme employed in the figure are following Worden et al. (2012; 2020).

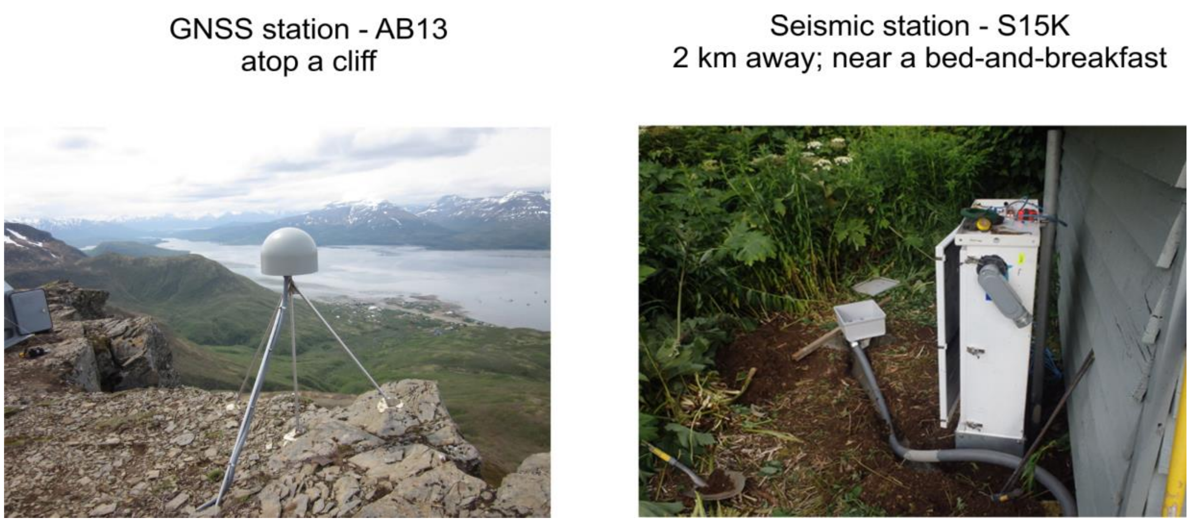

Figure S5: Site effects - 2 km apart: [Left] Location of GNSS station AB13 atop a cliff. Image credit: IRIS. [Right] Location of strong motion station AK.S15K ~2km away from AB13. Image credit: UNAVCO.